

Oxidative coupling of methane: catalytic behaviour assessment via comprehensive microkinetic modelling



V.I. Alexiadis, J.W. Thybaut*, P.N. Kechagiopoulos, M. Chaar, A.C. Van Veen, M. Muhler, G.B. Marin

Laboratory for Chemical Technology, Ghent University, Technologiepark 914, B-9052 Zwijnaarde, Belgium

ARTICLE INFO

Article history:

Received 15 November 2013

Received in revised form

19 December 2013

Accepted 23 December 2013

Available online 1 January 2014

Keywords:

Ethylene

Homogeneous–heterogeneous reaction network

Rare earth catalyst

LiMgO catalyst

ABSTRACT

A comprehensive microkinetic model, including catalyst descriptors, that accounts for thermal, homogeneous and catalytic, heterogeneous reaction steps in the oxidative coupling of methane has been used in the assessment of kinetic data acquired on different catalysts. The applicability of the model was extended from alkali magnesia catalysts represented by Li/MgO and Sn–Li/MgO, to a new class of materials, namely alkaline earth-promoted lanthana catalysts, represented by Sr/La₂O₃. To simulate adequately the large experimental dataset, acquired with the latter catalyst, the surface reaction network of the microkinetic model was expanded. The resulting model succeeded in adequately simulating the C₂, that is, ethane and ethene, production, both individually and as a lump during regression. It was found that the activity of Sr/La₂O₃, in terms of methane conversion, is 33 and five times higher than that of Li/MgO and Sn–Li/MgO, respectively. This is attributed mainly to the higher stability of adsorbed hydroxyl, the higher stability of adsorbed oxygen, and the higher active density of Sr/La₂O₃. The selectivity toward C₂ products was found to depend on the methyl radical sticking coefficient and the stability of the adsorbed oxygen and was the highest on the Sn-promoted LiMgO catalyst, that is, 70% at about 5% methane conversion at 1023 K, 190 kPa, and inlet molar CH₄/O₂ ratio of 4.

© 2014 Elsevier B.V. All rights reserved.

1. Introduction

The oxidative coupling of methane (OCM) to C₂ and higher hydrocarbons has been widely accepted as a promising route to upgrade natural gas since the pioneering work of Keller and Bhasin in the early 80s [1]. Since then, several metal oxides have been proven to be effective OCM catalysts, such as Li/MgO and Sn-doped Li/MgO [2,3], Sr-promoted rare earth (La, Ce, Pr, Nd, etc.) catalysts [4], Na–Mn–W/SiO₂ [5–8], and Sn–, Zr–, P–, S-doped Na–Mn–W/SiO₂ catalysts [8–11]. However, none of them has reached the stage of commercial implementation yet, since their performance in terms of C₂ yield remains relatively low, despite all progress made.

High-throughput experimentation combined with combinatorial chemistry is capable of evaluating a large number of candidate catalysts in a short period of time. However, relating catalyst descriptors in the latter approach only to synthesis parameters prevents deepening the fundamental understanding of the reaction. It has been suggested [12–14] that a microkinetic analysis would be a valuable guiding technique in the search for new catalysts by combinatorial chemistry. Microkinetic analyses allow

accounting for the fundamental catalytic surface chemistry in a kinetic model in the form of elementary steps and catalytic cycles. Catalyst descriptors incorporated into such models are, in principle, measured independently or calculated applying theoretical chemistry. Catalyst descriptors correspond to a physical or chemical property of the catalyst in interaction with the reacting species and potentially affect the reaction kinetics via pre-exponential factors, activation energies, or reaction enthalpies. The incorporation of the catalyst descriptors can take place through the implementation of thermodynamic relationships, for example, Born Haber cycles or Polanyi relationships [13,14], the latter more specifically exploiting the chemical similarity between various catalytic elementary steps. Due to these catalyst descriptors, the kinetic behaviour of an entire catalyst family, and even of various catalyst families, rather than of a single catalyst can be evaluated by the microkinetic model. Consequently, optimized catalyst descriptor values can be determined and related to novel catalyst compositions and/or structures [13,14]. The actual synthesis of these microkinetic model-based catalysts is the challenge to be met to close the loop in rational catalyst design [12–14].

The above-described approach can be adopted in the case of OCM, which is a complex reaction in which catalytic and gas phase reactions interact with each other [15], as depicted in Fig. 1. This figure constitutes an elaborated version of a literature-reported figure

* Corresponding author. Tel.: +32 9 331 1752.
E-mail address: Joris.Thybaut@UGent.be (J.W. Thybaut).

Nomenclature

Roman letters

b	the parameter vector containing the adjustable parameters
E_0	intrinsic activation barrier of a reaction family (kJ/mol)
$F_{\text{reactants}}$	flow rate of reactants ($\text{CH}_4 + \text{O}_2$) (mol/s)
p	pressure (kPa)
rf_i	reaction family i
S_i	selectivity toward product i (%)
T	temperature (K)
W	catalyst loading (kg)
X_i	conversion of reactant i (%)
y	observed molar fractions
\hat{y}	calculated molar fractions

Greek letters

α	transfer coefficient of a reaction family
ΔH	reaction enthalpy (kJ/mol)
$\sigma_{j,k}^{-1}$	element of the inverse of the error variance–covariance matrix

describing the OCM reaction [14]. The catalyst is activated through dissociative oxygen chemisorption and subsequently produces gas phase methyl radicals by hydrogen abstraction from methane. Methyl radicals can couple in the gas phase to form ethane, which in turn can be dehydrogenated into ethylene. However, they can also be oxidized toward undesired carbon oxides, CO, and CO_2 , in the gas phase as well as by interaction with the catalyst surface [16].

In the work of Couwenberg et al. [3], it was established that gas phase radicals are highly reactive and lead to irreducible mass transport limitations. This effectively means that the pellet size necessary to consider the internal concentration gradients as negligible is so small that it would lead to an unacceptable pressure drop over the catalyst bed. As a result, these transport limitations have to be explicitly accounted for during the determination of OCM kinetics. A one-dimensional, heterogeneous reactor model was specifically developed by Couwenberg et al. [2,3] to properly describe the interaction between elementary catalytic steps and gas phase steps. Sun et al. [14] expanded the surface reaction network, introducing reversible reaction steps and elaborating on the deep oxidation steps. Additionally, catalyst descriptors were introduced in the model, so as to facilitate knowledge extraction from high-throughput experiments. Recently, in the work by Thybaut et al. [13], the surface reaction network was further elaborated, including reaction steps accounting for the heterogeneous oxidation of ethylene.

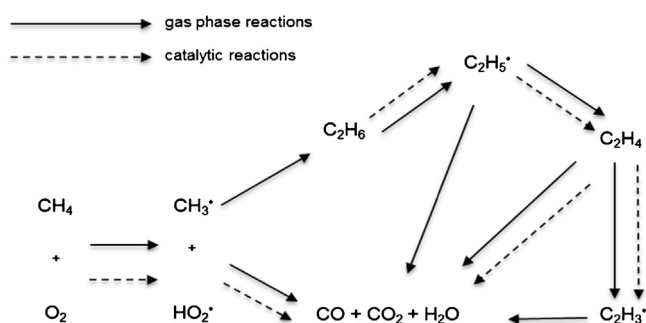


Fig. 1. Global reaction steps involved in OCM reaction, indicating their homogeneous and/or heterogeneous character.

Table 1

(a) Physical properties of the investigated catalysts.

Catalyst	Sr/La ₂ O ₃	Li/MgO	Sn–Li/MgO
Surface area ($\text{m}^2 \text{kg}^{-1}$)	2000	1000	2800
Porosity ($\text{m}^3 \text{m}^{-3}$)	0.27	0.29	0.27
Density ($\text{kg} \text{m}^{-3}$)	2300	2350	2300

(b) Operating conditions employed over the investigated catalysts.

Operating conditions	Sr/La ₂ O ₃	(Sn–)Li/MgO*
Pressure (kPa)	190	108–130
Temperature (K)	980–1180	947–1013
CH_4/O_2 ($\text{mol}_{\text{CH}_4} \text{mol}_{\text{O}_2}^{-1}$)	2–4	2–12
$W/F_{\text{reactants}}$ ($\text{kg s mol}^{-1}_{\text{reactants}}$)	0.2–1.2	2–12
N_2 dilution (%)	80	0
Radius of catalyst pellet (m)	1×10^{-4}	1.25×10^{-4}

*The experimentation has been reported previously [2,3].

In the current work, an enhanced version of the OCM microkinetic model [13] is presented, which aims at describing adequately large amounts of experimental data, produced over various catalyst families. The gas phase reaction network was adopted from Chen et al. [17], while the catalytic reaction network was enhanced compared to previous work [13] as elaborated in more detail in the recent work by Kechagiopoulos et al. [18]. The microkinetic model was incorporated into a one-dimensional heterogeneous reactor model. The overall model was employed to investigate the performance of catalysts, representative of two different catalyst families, that is, alkaline earth-promoted lanthana catalysts and alkali magnesia-based catalysts.

2. Procedures

2.1. Experimental

An extensive OCM experimental dataset was acquired over a Sr/La₂O₃ catalyst covering a wide range of operating conditions. A brief description is given of the Sr/La₂O₃ catalytic material, the experimental setup, and the employed operating conditions during the OCM experiments. Materials and procedures for the acquisition of literature data on Li/MgO and Sn–Li/MgO performances [2,3] are provided alongside for reference.

2.1.1. Catalyst

Alkaline earth-promoted La₂O₃ catalysts have been reported to be efficient catalytic materials in the OCM reaction [19,20]. Among these catalysts, the Sr-promoted ones have been found to exhibit superior performance in terms of activity as well as of selectivity to C_2 products. This has been attributed to the large number of strong basic sites and intermediate strength acid sites they contain [19]. Moreover, it was established that a low Sr to La ratio enhances the OCM activity and selectivity of the catalyst [19]. Hence, within the current study, the composition of the investigated catalyst was selected as 1wt% Sr/La₂O₃. Table 1a presents the main structural properties of this catalyst. The values correspond to the lined-out catalyst (see Section 2.1.3). The respective values for the MgO catalysts [14] are also shown in Table 1a. As can be easily observed, the investigated catalysts present similar physical properties. The low value of the surface area of Sr/La₂O₃ is in line with previous findings [19].

2.1.2. Setup

Experimental data for microkinetic model validation were acquired in a fixed bed reactor. Special attention was paid to operate the reactor in the plug-flow regime with minimal axial and radial temperature gradients and negligible pressure drop over the catalyst bed. The latter conditions justify the use of a one-dimensional

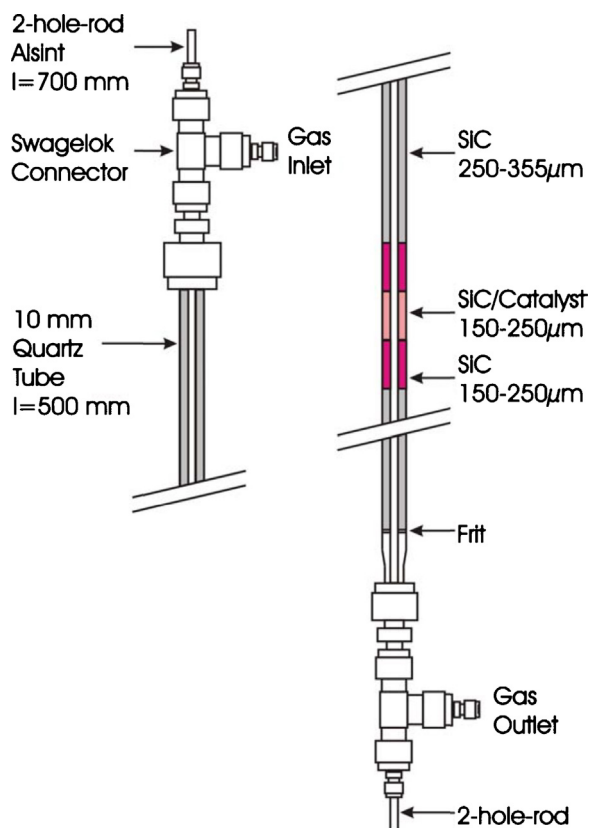


Fig. 2. Schematic of the reactor used in the OCM kinetic study on the $\text{Sr/La}_2\text{O}_3$ catalyst.

reactor model in the simulation of the experimental data using a detailed microkinetic model.

The tubular quartz reactor had an inner diameter of 7 mm (see Fig. 2). A 3-mm ceramic rod was aligned concentrically and contained two thermocouples, of which one was moved to collect axial temperature profiles. The other thermocouple uninterruptedly recorded the highest temperature in the catalytic zone. The latter was considered as the catalyst bed temperature. Radial temperature gradients were minimized by diluting the fixed bed with a high thermal conducting inert material such as silicon carbide (SiC). Its negligible blind activity and inertness with respect to $\text{Sr/La}_2\text{O}_3$ were verified during preliminary OCM experiments. The ratio of 1% $\text{Sr/La}_2\text{O}_3$ catalyst (150–250 μm) to SiC inert material (150–250 μm) was approximately 1/20. Even at such mass ratios between the catalyst and the inert material, the available catalytic surface area exceeds that of the inert material at least by a factor of 10. SiC in the same sieve fraction (150–250 μm , 1 g) enveloped the

catalytic zone to ensure a steady gas velocity profile. Void space in the reactor was minimized, that is, the gas preheating and cooling zones were filled with SiC in a larger sieve fraction (250–355 μm). Analysis of the effluent stream was done by means of a calibrated gas chromatograph ($\mu\text{-GC}$, Agilent Industries 3000A).

2.1.3. Operating conditions

The reproducibility of the kinetic measurements was ensured by applying a standardized pre-treatment routine. The initial state of the catalyst was defined by calcination in the reactor for 1 h at 850 °C in a flow of $3.7 \times 10^{-5} \text{ mol/s N}_2/\text{O}_2 = 80\%/20\%$.

Subsequent lining out of the catalyst consisted of sending $2.47 \times 10^{-4} \text{ mol/s N}_2$, $1.23 \times 10^{-5} \text{ mol/s CH}_4$, and $1.23 \times 10^{-5} \text{ mol/s O}_2$ over the catalyst. The temperature of the oven was raised from room temperature until reaching a catalyst hot-spot temperature of 850 °C. During lining out under severe conditions, the catalyst temperature decreased asymptotically to reach after 72 h on stream a nearly constant level. During OCM experiments, the concentration of reactive gas was maintained at 20% for safety reasons and the total pressure was fixed by means of a pressure controller.

Variable parameters were the inlet molar ratio of $\text{CH}_4:\text{O}_2$, the space time, calculated based on the sum of both reactant flow rates, that is, CH_4 and O_2 , and the catalyst temperature (see also Table 1b). High reactant flow rates were employed to avoid external mass transfer limitations to the largest possible extent. The maximum catalyst loading was set at 75 mg to keep oxygen conversion below 90% at a temperature of 850 °C. The corresponding space times are defined accordingly. Catalyst temperatures were kept below 900 °C to ensure long-term stability in kinetic experimentation. A dataset consisting of 176 observations was compiled.

2.2. Modelling

The microkinetic model was in the first instance validated against data produced over the $\text{Sr/La}_2\text{O}_3$ catalyst. Subsequently, also the literature data on Li/MgO , Sn-Li/MgO [2,3] were reassessed, given the enhancements made to the microkinetic model with respect to the catalytic reaction network and the reactor model. Below is a brief discussion of these enhancements as required for the proper understanding of the current work. A more elaborate description is discussed separately [18].

2.2.1. Reaction kinetics

The gas phase reaction network containing 39 elementary steps was adopted from previous work [2,3,13,14,21]. The catalytic reaction network was modified. The 26 elementary steps on the catalyst surface considered in the current version of the microkinetic model are shown in Table 2. The depicted catalytic steps can be classified into three types, that is, adsorption steps (40, 45–46, 51–53, 65),

Table 2
Catalytic elementary steps considered in the comprehensive microkinetic OCM model presented in this work.

No.	Adsorption steps	No.	Eley–Rideal steps	No.	Surface reaction steps
40	$\text{O}_2 + 2^* \rightleftharpoons 2\text{O}^*$	41	$\text{CH}_4 + \text{O}^* \rightleftharpoons \text{CH}_3 \cdot + \text{OH}^*$	44	$2\text{OH}^* \rightleftharpoons \text{H}_2\text{O}^* + \text{O}^*$
45	$\text{H}_2\text{O}^* \rightleftharpoons \text{H}_2\text{O} + ^*$	42	$\text{C}_2\text{H}_4 + \text{O}^* \rightleftharpoons \text{C}_2\text{H}_3 \cdot + \text{OH}^*$	47	$\text{CH}_3\text{O}^* + \text{O}^* \rightleftharpoons \text{CH}_2\text{O}^* + \text{OH}^*$
46	$\text{CH}_3 \cdot + \text{O}^* \rightleftharpoons \text{CH}_3\text{O}^*$	43	$\text{C}_2\text{H}_6 + \text{O}^* \rightleftharpoons \text{C}_2\text{H}_5 \cdot + \text{OH}^*$	48	$\text{CH}_2\text{O}^* + \text{O}^* \rightleftharpoons \text{HCO}^* + \text{OH}^*$
51	$\text{CO} + ^* \rightleftharpoons \text{CO}^*$	56	$\text{C}_2\text{H}_5 \cdot + \text{O}^* \rightleftharpoons \text{C}_2\text{H}_4 + \text{OH}^*$	49	$\text{CHO}^* + \text{O}^* \rightleftharpoons \text{CO}^* + \text{OH}^*$
52	$\text{CO}_2 + ^* \rightleftharpoons \text{CO}_2^*$	57	$\text{CH}_3\text{O} \cdot + \text{O}^* \rightleftharpoons \text{CH}_2\text{O} + \text{OH}^*$	50	$\text{CO}^* + \text{O}^* \rightleftharpoons \text{CO}_2^* + ^*$
53	$\text{C}_2\text{H}_4 + \text{O}^* \rightleftharpoons \text{C}_2\text{H}_4\text{O}^*$	58	$\text{CH}_2\text{O} + \text{O}^* \rightleftharpoons \text{CHO} \cdot + \text{OH}^*$	54	$\text{C}_2\text{H}_4\text{O}^* + \text{O}^* \rightleftharpoons \text{C}_2\text{H}_3\text{O}^* + \text{OH}^*$
65	$\text{HO}_2 \cdot + ^* \rightleftharpoons \text{OH} \cdot + \text{O}^*$	59	$\text{CHO} \cdot + \text{O}^* \rightleftharpoons \text{CO} + \text{OH}^*$	55	$\text{C}_2\text{H}_3\text{O}^* + \text{O}^* \rightleftharpoons \text{CH}_2\text{O}^* + \text{HCO}^*$
		60	$\text{H}_2 + \text{O}^* \rightleftharpoons \text{H} \cdot + \text{OH}^*$		
		61	$\text{H}_2\text{O}_2 + \text{O}^* \rightleftharpoons \text{HO}_2 \cdot + \text{OH}^*$		
		62	$\text{OH} \cdot + \text{O}^* \rightleftharpoons \text{O} \cdot + \text{OH}^*$		
		63	$\text{H}_2\text{O} + \text{O}^* \rightleftharpoons \text{OH} \cdot + \text{OH}^*$		
		64	$\text{HO}_2 \cdot + \text{O}^* \rightleftharpoons \text{O}_2 + \text{OH}^*$		

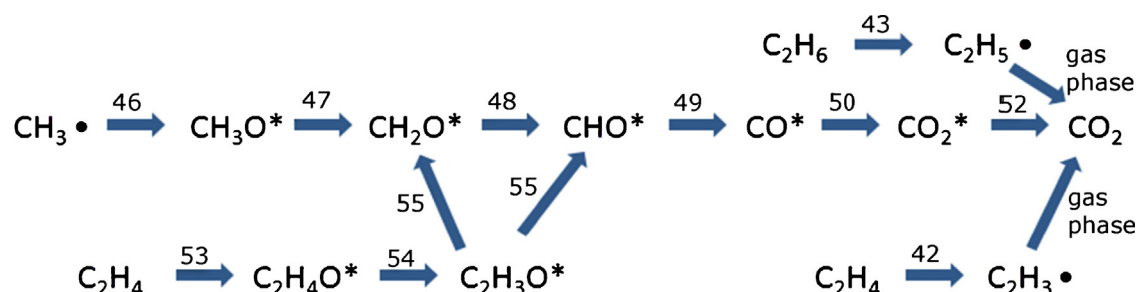


Fig. 3. Catalytic reaction pathways accounted for in the comprehensive microkinetic model to simulate CO₂ formation from C₂ precursor and C₂ gas phase species.

Eley–Rideal reactions (41–43, 56–64), and surface reactions (44, 47–50, 54–55).

Compared with the catalytic reaction network previously suggested [13], ten elementary steps were added (56–65), highlighted in Table 2, nine of which (56–64) account for H-atom abstraction from gas phase species according to an Eley–Rideal mechanism [22]. Step 65 accounts for the adsorption of hydroperoxy radicals on the catalyst surface and replaces the previously considered pseudo-homogeneous step, $4\text{HO}_2 \cdot \xrightarrow{\text{surf}} 3\text{O}_2 + 2\text{H}_2\text{O}$ [13].

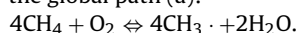
During OCM, carbon dioxide is virtually exclusively produced via catalytic reactions [2,3,14]. Several potential reaction pathways and corresponding elementary steps have been proposed for the catalytic CO₂ formation [14]. In particular, the current microkinetic model accounts for the conversion of the C₂ precursor and C₂ desired gas phase species to CO₂ through three reaction pathways involving at least one catalytic step (see also Fig. 3):

- Methyl radical scavenging followed by the sequential hydrogen abstraction from methoxy species on the catalyst (steps 46–50, 52).
- Hydrogen abstraction from ethane and ethylene (steps 42–43), leading to radicals that are oxidized to CO₂ in the gas phase.
- Heterogeneous oxidation of ethylene via an adsorption step, followed by a hydrogen abstraction and C–C bond cleavage (steps 53–55).

2.2.2. Reactor model

The microkinetic model was implemented in a one-dimensional heterogeneous reactor model, which explicitly accounts for the irreducible mass transfer limitations induced by the high reactivity of the produced radicals. It also describes diluent effects on the relative contribution by heterogeneous and homogeneous reactions due to a changing catalyst/solid surface to interstitial and intraparticle gas volume in the reactor. The current reactor model constitutes an enhanced version of the previously developed one [13,14]. Intraparticle surface coverage profiles can now be determined for all the adsorbed species [18], whereas previous versions of the reactor model were limited to average coverage values.

The net production rates of the components participating in the surface reaction network, as required by the reactor model, were calculated using 16 global reaction paths [2,23] comprising the 26 catalytic elementary steps reported in Table 2. As an example, the catalytic formation of methyl radicals from methane is described by the global path (a):



As can be seen in Table 3, this path can be constructed by the summation of the elementary steps 40, 41, 44, and 45. Among these, step 41 has to take place four times for the global path (a) to proceed once, while it is not involved in any other global path. Hence, the reaction rate of path (a) is calculated as: $r_a = 0.25 r_{41}$.

A more detailed description of the reactor model is beyond the scope of the current work and is discussed separately [18].

Table 3

Four-step catalytic cycle constituting the global reaction path for methyl radical production in OCM.

1 ×	$\text{O}_2 + 2^* \rightleftharpoons 2\text{O}^*$	ΔH_{40}
4 ×	$\text{CH}_4 + \text{O}^* \rightleftharpoons \text{CH}_3 \cdot + \text{OH}^*$	ΔH_{41}
2 ×	$\text{OH}^* + \text{OH}^* \rightleftharpoons \text{H}_2\text{O}^* + \text{O}^*$	ΔH_{44}
2 ×	$\text{H}_2\text{O}^* \rightleftharpoons \text{H}_2\text{O} + ^*$	ΔH_{45}
Sum	$4\text{CH}_4 + \text{O}_2 \rightleftharpoons 4\text{CH}_3 \cdot + 2\text{H}_2\text{O}$	$\Delta H_{\text{path(a)}}$

2.2.3. Model parameters

Rate coefficients of the catalytic steps, presented in Table 2, are calculated from the respective pre-exponential factors and activation energies. Collision theory was used to estimate the maximum value of the pre-exponential factors of the steps involving interaction of a gas phase species with the catalyst surface [14,24], that is, adsorption and Eley–Rideal steps. The pre-exponential factors for the adsorption steps were corrected with separate initial sticking probabilities (S_0) representing the probability that the respective molecules effectively remain trapped on a clean catalyst surface. These initial sticking probabilities were considered as catalyst descriptors. The maximum value of the pre-exponential factors in Eley–Rideal steps was not corrected, since these steps are activated in contrast to the adsorption steps and, hence, the effect of pre-exponential factors on the rate coefficients is affected by the corresponding activation energy. Pre-exponential factor values for the surface reaction steps (see Table 2) were determined by transition-state theory. It is known that an order of magnitude determination of these pre-exponential factors typically suffices because of the dominating and potentially compensating effect of the exponential term containing the activation energy on the rate coefficient [25]. Hence, the a priori determined pre-exponential factors were left unchanged at values reported previously [13,14,25]. Note that the surface reaction rates exhibit a square dependence on the active site density and, hence, will decrease more significantly with decreasing active site density compared to the rates of the Eley–Rideal steps.

Activation energies of the catalytic steps, as reported in Table 2, were obtained from the surface thermodynamics via Polanyi relationships. Surface thermodynamics were determined by the catalyst descriptors in the microkinetic model. Thermodynamic consistency was preserved through the considered catalytic cycles, which allow expressing reaction enthalpies for various elementary steps as a function of a limited number of unknown catalyst descriptors which can subsequently be obtained by regression [14,26,27]. The current microkinetic model accounts for more catalytic cycles than strictly required to simulate the OCM behaviour on a single catalyst. The values of the respective catalyst descriptors, identified as discussed above, determine the contribution of each catalytic cycle to the overall OCM performance.

All adsorption steps were considered to be non-activated. As shown in Table 4, all Eley–Rideal steps were grouped into a single reaction family (rf₁), while the surface reaction steps were

subdivided into four reaction families, accounting for H-atom abstraction (rf_2), recombination of hydroxyls (rf_3), catalytic oxidation of CO (rf_4), and C–C bond scission (rf_5), respectively. In particular, steps 44, 50, and 55 could not be classified into reaction family 2 as the structural variation in these reactions is different from the other surface reaction steps. Hence, for the sake of generality, these three steps were considered as separate reaction families [13,14]. Each reaction family (rf_1 – rf_5) has a specific set of the Polanyi parameters α and E_0 . Values of α were taken from literature [25,28–30]. The reference activation energies, E_0 , were defined as kinetic descriptors and determined by regression. The extension of the catalytic reaction network has required a re-estimation of these kinetic descriptors compared to previous work. The number of kinetic descriptors remained unchanged as newly incorporated activated steps (56–64) were classified in an existing family (rf_1).

Two new catalyst descriptors were incorporated into the model to render it more detailed and accurate, that is, the chemisorption enthalpy of vinyloxy radical (related to the steps 54, 55) and the initial sticking probability of ethylene (step 53). A previous model [13] fixed the chemisorption enthalpy of vinyloxy radicals a priori, while the initial sticking probability of ethylene was assumed equal to unity. In summary, the corresponding set of catalyst descriptors in the microkinetic model for methane oxidative coupling can, hence, be classified as follows:

- Reaction enthalpy of hydrogen abstraction from CH_4 (D_1).
- Chemisorption heats of O_2 , CH_2O , HCO , CO , CO_2 , H_2O , C_2H_4O , C_2H_3O (D_2 – D_9).
- Initial sticking probabilities of O_2 , CH_3 , CO , CO_2 , H_2O , C_2H_4 (D_{10} – D_{15}).
- Density of active sites (D_{16}).

The methane hydrogen abstraction enthalpy, that is, D_1 in combination with the oxygen chemisorption enthalpy, that is, D_2 determines the stability of the hydroxyl species on the catalyst surface. The latter affects significantly the methane activation and the C_2 selectivity, mainly via the formation of adsorbed atomic oxygen (step 44, Table 2). The chemisorption enthalpy of OH^- species can be obtained by considering the following elementary steps:

1 x	$H \cdot + OH \cdot \rightleftharpoons H_2O$	ΔH_A
1 x	$CH_4 \rightleftharpoons CH_3 \cdot + H \cdot$	ΔH_B
–1 x	$CH_4 + O^* \rightleftharpoons CH_3 \cdot + OH^*$	ΔH_{41}
–1 x	$OH^* + OH^* \rightleftharpoons H_2O^* + O^*$	ΔH_{44}
–1 x	$H_2O^* \rightleftharpoons H_2O + ^*$	ΔH_{45}
Sum	$OH \cdot + ^* \rightleftharpoons OH^*$	ΔH_{OH^*}

According to Hess' law, the chemisorption enthalpy of hydroxyl radicals is determined as:

$$\Delta H_{OH^*} = \Delta H_A + \Delta H_B - \Delta H_{41} - \Delta H_{44} - \Delta H_{45} \quad (1)$$

The reaction enthalpies ΔH_A and ΔH_B are calculated from thermodynamic data. According to Table 3, the hydroxyls recombination enthalpy, ΔH_{44} , is determined as follows:

$$\Delta H_{44} = 0.5 \Delta H_{path(a)} - \Delta H_{45} - 2 \Delta H_{41} - 0.5 \Delta H_{40} \quad (2)$$

The reaction enthalpies ΔH_{40} and ΔH_{45} have been defined as descriptors D_2 and D_7 , respectively, while the reaction enthalpy of the global reaction path, $\Delta H_{path(a)}$, can be calculated from thermodynamic data. The summation of Eqs. (1) and (2) leads to the following equation:

$$\Delta H_{OH^*} = \Delta H_A + \Delta H_B - \Delta H_{path(a)} + \Delta H_{41} - 0.5 \Delta H_{40} \quad (3)$$

Equation (3) illustrates that a more pronounced endothermicity of hydrogen abstraction from methane, that is, a more positive

ΔH_{41} , results in an equivalent decrease in the hydroxyl stability on the catalyst surface, that is, less negative ΔH_{OH^*} .

2.2.4. Parameter estimation

Parameter estimation was performed using the Rosenbrock methodology [31] for the initial minimization of the objective function followed by a Levenberg–Marquardt algorithm, that is, ODRPACK-package version 2.01 [32] for the final optimization. The objective function used in the model is the weighed sum of the squared residuals, $S(b)$, between the observed, y , and calculated, \hat{y} , molar fractions at the reactor outlet:

$$S(b) = \sum_{j=1}^{nresp} \sum_{k=1}^{nobs} \sigma_{j,k}^{-1} \sum_{i=1}^n (y_{i,j} - \hat{y}_{i,j})(y_{i,k} - \hat{y}_{i,k}) \xrightarrow{b} \min \quad (4)$$

where b is the parameter vector containing the adjustable parameters; $\sigma_{j,k}^{-1}$ is an element of the inverse of the error variance–covariance matrix, which is calculated from replicate experiments or estimated from the observed and calculated molar fractions at the reactor outlet. The objective function S was minimized by adjusting the model parameter vector b . The estimated parameters are the catalyst and kinetic descriptors as discussed in Section 2.2.3.

The initial guesses for the catalyst descriptors were chosen within the range of physically realistic values. For instance, the adsorption heat of CO_2 on alumina is reported to be approximately 70 kJ/mol [33] and the adsorption heat of CO, measured on various metal surfaces, ranges between 60 and 180 kJ/mol [34]. Furthermore, the adsorption heat of water can reach up to 65 kJ/mol [35], while the adsorption heat of O_2 on metal oxides is lower than 300 kJ/mol [36]. These values were used as constraints for the catalyst descriptors. The molar fractions of methane, oxygen, ethylene, ethane, carbon monoxide, and carbon dioxide at the reactor outlet were used as responses in the parameter estimation procedure.

3. Results and discussion

3.1. Experimental

3.1.1. Sr/La_2O_3

A large dataset comprising 176 experimental points was produced over Sr/La_2O_3 as part of the current work. Fig. 4 depicts the effect of the catalyst temperature on the conversion of the reactants and selectivities toward C_2 products and carbon oxides as a function of the space time. The total pressure and inlet molar methane to oxygen ratio were fixed at 190 kPa and 4, respectively. As expected, methane and oxygen conversions increased with temperature and space time. The maximum methane and oxygen conversion were 21.5 and 93% observed at 1123 K and $1.2 \text{ kg s mol}^{-1}_{\text{reactants}}$ under the investigated experimental conditions. As shown in Fig. 4, the ethane selectivity appeared to stabilize between 20 and 25%, while the ethylene selectivity increased with temperature and space time reaching a maximum of 14.5%. The formation of secondary ethylene from primary ethane is enhanced at these conditions, while preserving the ethane selectivity and simultaneously avoiding significant further consecutive oxidation to carbon oxides.

Interestingly and against intuition, the selectivity toward C_2 products increases slightly with conversion. At high conversion with increased formation of carbon oxides, in particular CO_2 , the selectivity was significantly determined by the catalytic reactions. This is evident from the evolution of selectivities toward CO and CO_2 , in Fig. 4. The CO selectivity decreases with conversion, since carbon monoxide is mainly generated in the gas phase, while the opposite holds true for CO_2 , which is mainly produced via

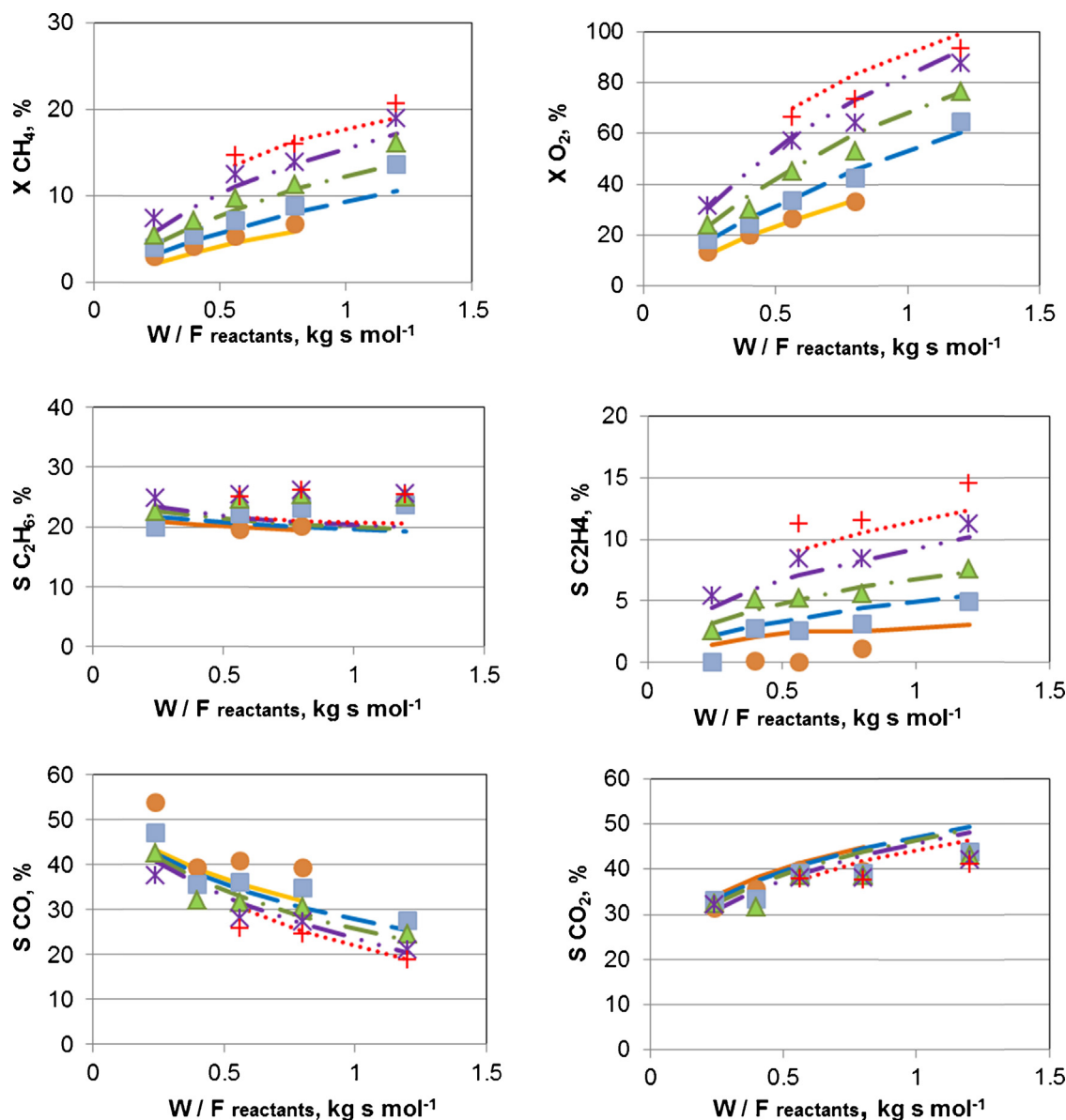


Fig. 4. Conversions and selectivities over Sr/La₂O₃ vs. space time of reactants at five catalyst temperatures. Experimental conditions: $p = 190$ kPa, inlet molar CH₄/O₂ ratio = 4, and N₂ dilution of 80%. Experimental symbols and simulation curves: (●) and (—): 1023 K; (■) and (---): 1048 K; (▲) and (· · ·): 1073 K; (*) and (· · · ·): 1098 K; (+) and (· · · · ·): 1123 K. Calculated conversions and selectivities were produced using the model described in Section 2.2 and the values of E_0 and catalyst descriptors are listed in Tables 4 and 5, respectively.

reactions on the catalyst surface. Furthermore, CO selectivity seems to be more temperature dependent than that of CO₂.

When product selectivities are extrapolated to zero space time and, hence, to zero conversion, the ethylene selectivity asymptotically approaches zero, indicating that ethylene is, indeed, a secondary product. On the other hand, the selectivities toward C₂H₆, CO, and CO₂ approach a finite value significantly different from zero, showing that these components are primary products of the heterogeneously catalyzed OCM.

3.1.2. Comparison between Sr/La₂O₃ and Li-based MgO catalysts

Literature-reported OCM data [2,3] on 30 and 40 experimental points produced over Li/MgO and Sn–Li/MgO, respectively, were employed for assessing the performance of an alkali manganese catalyst and its Sn-promoted version. Note that a significantly wider range of space times, that is, between 2 and 12 kg s mol^{−1}_{reactants}, was used on the (Sn)LiMgO catalyst compared to the Sr/La₂O₃ catalyst (see also Table 1).

Performances of the above three catalysts are compared in terms of methane conversions and C₂ selectivities presented as a function of space time in Fig. 5. All the experimental data have been acquired at an identical catalyst temperature of 1023 K. The applied methane to oxygen ratio of 3.5 was slightly lower in the case of Sn–Li/MgO, compared to the other two catalysts, for which a ratio of 4 was employed. Moreover, the total pressure was close to atmospheric in the cases of the Li-based MgO catalysts, while it was slightly higher in the case of Sr/La₂O₃ catalyst, that is, 190 kPa. The experiments over the latter catalyst were conducted under 80% inert gas (N₂) dilution, while in the case of the former catalysts, there was no dilution of the feed gas.

Even though the space time range is not the same for all the investigated catalysts, it is clear from Fig. 5 that Li/MgO is the by far least active catalyst reaching only a maximum methane conversion of 3%. The maximum methane conversion obtained with Sn–Li/MgO amounted to 22.8%. The C₂ selectivities over both catalysts were rather similar ranging between 50 and 55%.

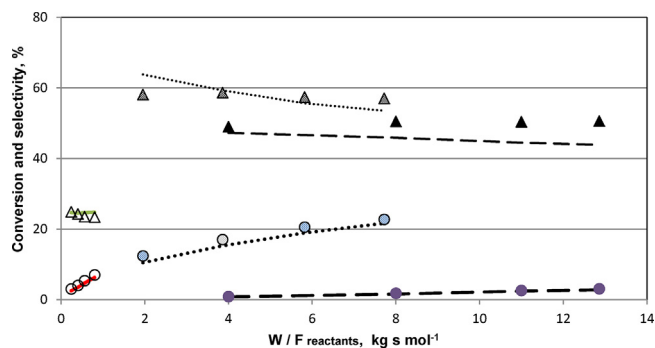


Fig. 5. Methane conversion and C_2 selectivity vs. space time. Lines: simulated conversions, thick lines and selectivities, thin lines; (dashed line) Li/MgO; (dotted line) Sn-Li/MgO; (full line) Sr/La₂O₃; symbols-experiments: (●) conversion and (▲) selectivity; closed symbols: Li/MgO; grey symbols: Sn-Li/MgO, open symbols: Sr/La₂O₃. Experimental conditions: Li/MgO: $T = 1023$ K, $p = 112$ kPa, inlet molar CH_4/O_2 ratio = 4, no N_2 dilution; Sn-Li/MgO: $T = 1023$ K, $p = 117$ kPa, inlet molar CH_4/O_2 ratio = 3.5, no N_2 dilution; Sr/La₂O₃: $T = 1023$ K, $p = 190$ kPa, inlet molar CH_4/O_2 ratio = 4, N_2 dilution: 80%. Simulation results were obtained with the model described in Section 2.2 and the values of E_0 and catalyst descriptors are listed in Tables 4 and 5, respectively.

Methane conversions obtained with Sr/La₂O₃ and Sn-Li/MgO follow similar trends as a function of space time. However, the experiments with the latter catalyst were carried out at more concentrated conditions and slightly lower CH_4/O_2 ratio, which are both expected to promote methane conversion. With respect to catalytic activity, the three catalysts can, hence, be ranked as follows from high to low: Sr/La₂O₃ > Sn-Li/MgO > Li/MgO. The C_2 selectivity, however, is clearly higher on Sn-Li/MgO than on Sr/La₂O₃ under the respective OCM experimental conditions.

3.2. Model validation/regression

The model was assessed describing initially the experimental data produced over the Sr/La₂O₃ catalyst. A reduced dataset of 53 experiments was used in the parameter estimation procedure to minimize the computational time. The estimated values of the parameters were then employed for the simulation of all 176 experiments. Fig. 6a presents the parity diagrams for CH_4 , O_2 , and lumped C_2 products.

As can be clearly seen, the microkinetic model yielded a very good agreement with the experimental data on the Sr/La₂O₃ catalyst over the complete range of experimental conditions.

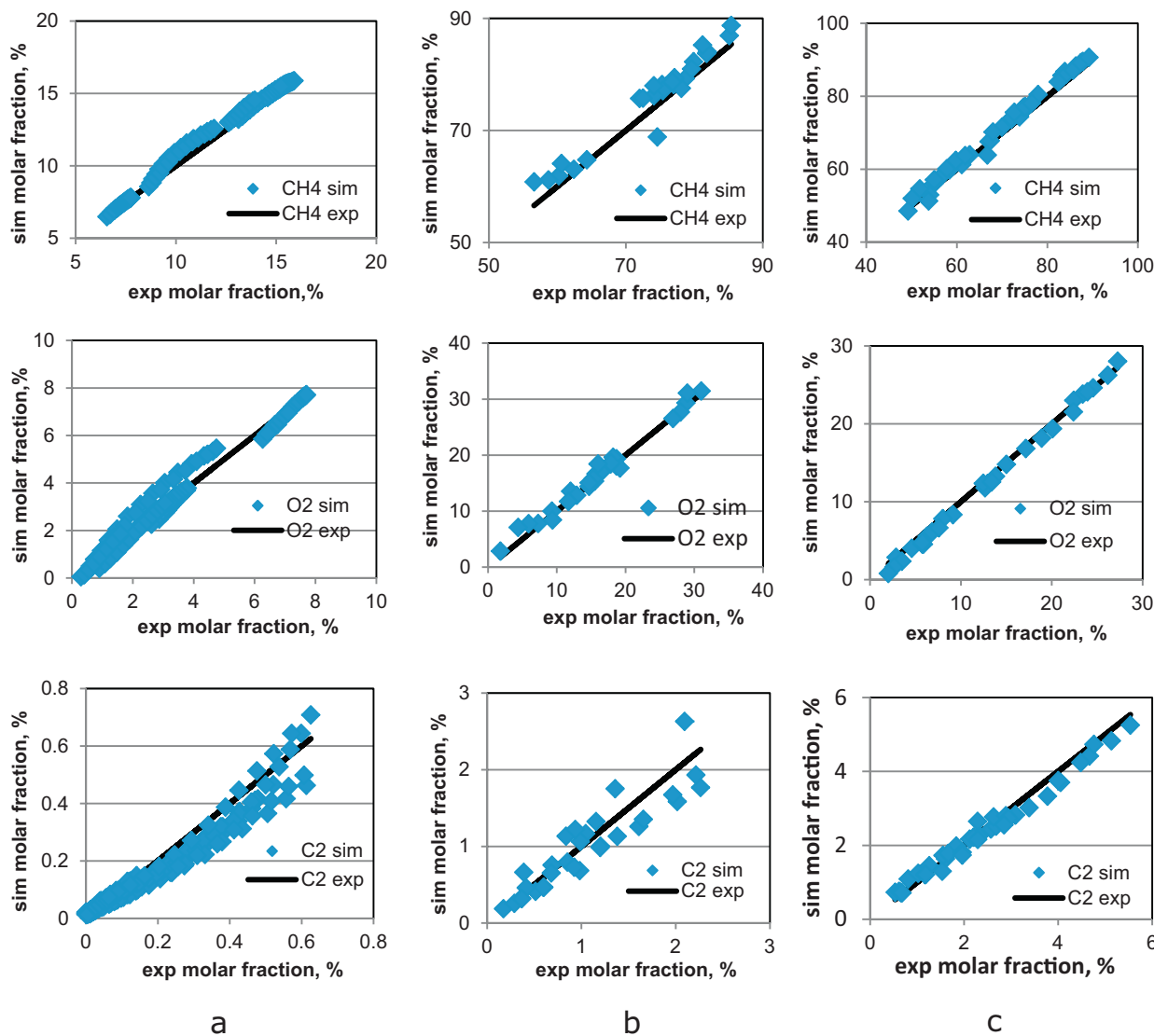


Fig. 6. Parity diagrams for CH_4 , O_2 , and lumped C_2 over (a) Sr/La₂O₃, (b) Li/MgO, and (c) Sn-Li/MgO. The experimental conditions are summarized in Table 1. Simulation results were obtained with the model described in Section 2.2 and the values of E_0 and catalyst descriptors are listed in Tables 4 and 5, respectively.

Table 4

Reaction families and corresponding parameters employed in the Polanyi relationships considered in the comprehensive microkinetic OCM model.

	Reaction family	α	E_0 (kJ/mol)
rf ₁	Hydrogen abstraction by Eley–Rideal reaction (steps 41–43, 56–64)	0.75 [30]	96.8 ± 3.4
rf ₂	Hydrogen abstraction by surface reaction (steps 47–49, 54)	0.50 [29]	141.3
rf ₃	Recombination of hydroxyls (step 44)	0.65 [25]	130.2 ± 7.2
rf ₄	CO oxidation on the surface (step 50)	0.26 [28]	67.6
rf ₅	C–C cleavage on the surface (step 55)	0.97 [28]	185.7

Furthermore, the outlet molar fractions of carbon oxides as well as those of water, not shown in Fig. 6a, were adequately simulated by the microkinetic model. The parameter estimates obtained for the intrinsic activation barriers, E_0 , of the five reaction families along with the catalyst descriptors are reported in Tables 4 and 5, respectively.

All the catalytic and kinetic descriptors summarized in Section 2.2.3 were varied during initial regression. The model was found to be most sensitive to the following four catalyst descriptors: the H-atom abstraction enthalpy from methane (D_1), the chemisorption heat of oxygen (D_2), and the active site density (D_{16}) in addition to the initial sticking probability of CH_3 radicals on the surface (D_{11}). Regarding kinetic descriptors, E_0 , the model was most sensitive to the H-atom abstraction via Eley–Rideal reaction (rf₁) and recombination of hydroxyl species (rf₃), respectively (see Table 4). The values of the remaining catalyst and kinetic descriptors were fixed at the values obtained, during the preliminary parameter adjustment. The values reported in Table 4 for the kinetic descriptors, E_0 , are different from the ones previously reported [13,14], indicating the necessity to re-evaluate them after the modifications made on the catalytic reaction network (see also Section 2.2.1). The optimized catalyst descriptor values for Sr/La₂O₃ are physically realistic, since they lie within the literature-reported boundaries, as mentioned in Section 2.2.4, and are also statistically significant (see Table 5).

The maximum absolute value among the binary correlation coefficients amounted to 0.85 and occurred between the reaction enthalpy of methane hydrogen abstraction D_1 and the active sites density D_{16} . Such a value allows concluding that there is no significant correlation between the adjustable parameters. The high F value for the global significance of the regression of 945.3 illustrates the model's adequacy.

Fig. 4 compares the simulated conversions and product selectivities to the respective experimental values at different space times and catalyst temperatures. The model describes clearly adequate methane and oxygen conversions as well as the selectivity toward C_2 and carbon oxides. It illustrates that a one-step oxygen

adsorption suffices to adequately simulate the experimental data and gives confidence in the constructed mechanism and the corresponding model parameters. In particular, the accurate simulation of the selectivity toward CO_2 shows that the adopted catalytic reaction pathways shown in Fig. 3 contribute decisively to the adequate overall carbon dioxide production.

The previous model [14] did not succeed in describing adequately this large experimental dataset, acquired over the catalyst Sr/La₂O₃. In particular, ethane production was constantly overestimated. The less pronounced ethane formation as simulated by the current version of the model is a result of the catalytic conversion of ethane into ethylene through successive hydrogen atom abstraction steps, that is, 43 and 56 (Table 2). The production trend of the C_2 components is captured well by the model, both individually, as seen in Fig. 7, and certainly when lumped (Fig. 6a).

To assess the distinct activity and selectivity patterns in the performance of the three investigated catalysts (see also Fig. 5), the experimental data acquired over the two Li-based catalysts were also simulated by employing the herein reported model. During the regression analysis, only the four aforementioned descriptors, D_1 , D_2 , D_{11} , and D_{16} (see Table 5) were allowed to vary. Fig. 6b and c presents the parity diagrams for methane, oxygen, and C_2 products as a lump. It is clearly seen from Fig. 6b and c that the microkinetic model produced an adequate agreement with the experimental data over each of the two catalysts despite the limited number of adjustable parameters. Moreover, as can be seen in Fig. 5, the model can simulate correctly conversion and selectivity trends over the Li/MgO and Sn-doped Li/MgO catalysts.

The F value for the global significance of the regression of the data over the Li/MgO and Sn-Li/MgO was 352 and 834, respectively, further demonstrating the model's adequacy. Moreover, all descriptor values that have been obtained again lie within physically realistic constraints and give confidence in the constructed reaction network and the methodology applied for the determination of model parameters. As observed in Table 5, both MgO catalysts exhibit higher D_1 and lower D_2 , D_{11} , and D_{16} than the

Table 5Catalyst descriptors estimates pertaining to Sr/La₂O₃, Li/MgO, and Sn-Li/MgO in the comprehensive microkinetic model for OCM.

	Catalyst descriptor	Unit	Sr/La ₂ O ₃	Li/MgO	Sn-Li/MgO
D_1	Reaction enthalpy of hydrogen abstraction from CH_4	(kJ/mol)	44.4 ± 0.2	91.2 ± 0.2	56.6 ± 0.8
D_2	Chemisorption heat of O_2	(kJ/mol)	119.5 ± 3.5	73.6 ± 2.2	60.54 ± 2.6
D_3	Chemisorption heat of CH_2O	(kJ/mol)		123.1	
D_4	Chemisorption heat of HCO	(kJ/mol)		141.1	
D_5	Chemisorption heat of CO	(kJ/mol)		74.4	
D_6	Chemisorption heat of CO_2	(kJ/mol)		87	
D_7	Chemisorption heat of H_2O	(kJ/mol)		34.8	
D_8	Chemisorption heat of $\text{C}_2\text{H}_4\text{O}$	(kJ/mol)		42.4	
D_9	Chemisorption heat of $\text{C}_2\text{H}_3\text{O}$	(kJ/mol)		92.6	
D_{10}	Initial sticking probability of O_2			0.56	
D_{11}	Initial sticking probability of CH_3		6.49 ± 0.5 × 10 ⁻⁴	1.19 ± 0.0002 × 10 ⁻⁴	6.22 ± 0.1 × 10 ⁻⁵
D_{12}	Initial sticking probability of CO			5.66 × 10 ⁻⁵	
D_{13}	Initial sticking probability of CO_2			1.54 × 10 ⁻²	
D_{14}	Initial sticking probability of H_2O			7.65 × 10 ⁻²	
D_{15}	Initial sticking probability of C_2H_4			5.48 × 10 ⁻⁵	
D_{16}	Density of active sites	(mol/m ²)	9.84 ± 1 × 10 ⁻⁶	4.33 ± 0.009 × 10 ⁻⁷	1.33 ± 0.03 × 10 ⁻⁶

Value ± 95% confidence interval. Final weighted sums of squares = 6.28; F value for significance of the regression = 945.3; F tabulated value = 3.36.

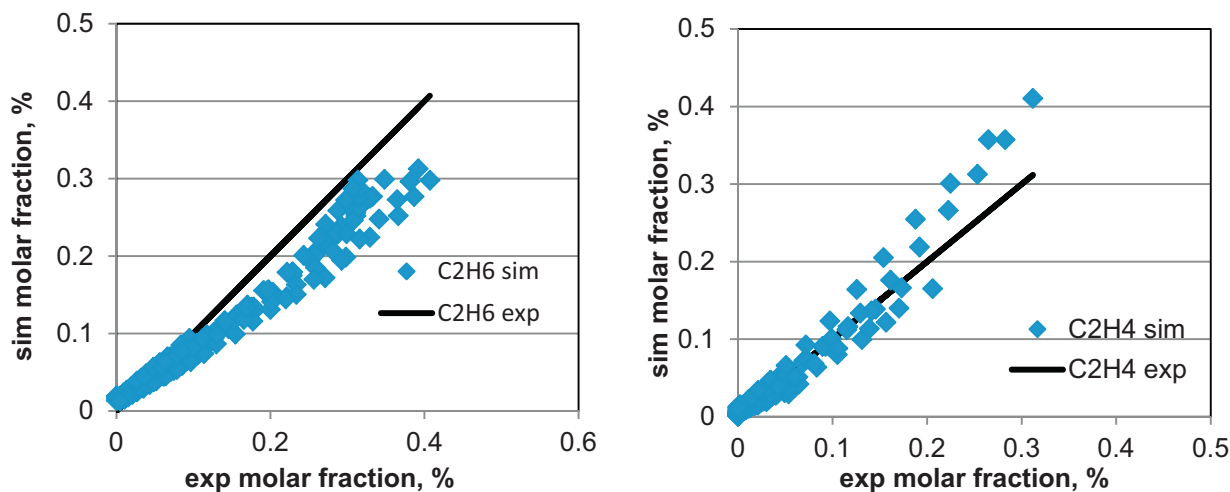


Fig. 7. Parity diagrams for ethane and ethylene over Sr/La₂O₃. The experimental conditions are summarized in Table 1. Simulation results were obtained with the model described in Section 2.2 and the values of E_0 and catalyst descriptors are listed in Tables 4 and 5, respectively.

Sr/La₂O₃ catalyst. This observation depicts the different physico-chemical properties of the three investigated catalysts and explains their distinct OCM performances, as illustrated in Fig. 5, see also the next section.

3.3. Interpretation and quantification of the experimental differences over Sr/La₂O₃ and the Li-based MgO catalysts

As mentioned in Section 2.2.3, the methane hydrogen abstraction reaction enthalpy, D_1 , corresponding to step 41 in Table 2, is related to the chemisorption enthalpy of OH[−] species. Comparison of the D_1 regressed values, pertaining to the three investigated catalysts (see Table 5), shows that this step is highly endothermic in the case of Li–MgO catalyst. As discussed in Section 2.2.3 (see Eq. 3), this effectively means that hydroxyl species are less stable on this catalyst, that is, their chemisorption heat decreases, and within the range of the catalyst descriptor values presented in Table 5, this was found to lead to a decrease in catalytic methane conversion. Indeed, the positive difference in the activation energies between the forward and the backward direction of step 41 increases with endothermicity, slowing down methane conversion. Furthermore, the density of the active sites (D_{16}) on this catalyst is much lower than in the case of Sr/La₂O₃ and Sn–Li/MgO catalysts, implying the limited contribution of the catalytic reactions to the overall OCM reaction rate. These findings reveal the intrinsic reason for the low activity of Li–MgO catalyst illustrated in Fig. 5.

The value of the initial sticking probability of CH₃ radicals (D_{11} , Table 5) has crucial importance to rationalize the effect on the C₂ selectivity of the Sn addition to the Li/MgO catalyst under OCM reaction conditions. As it is readily seen, the value of D_{11} on the Sn-promoted catalyst is lower than on the non-promoted one. The increase in D_{16} simultaneously with the decrease in D_{11} and D_1 provide a comprehensive explanation for the promoting effect of Sn: the C₂ selectivity is increased because of the decrease in the oxidation rate of methyl radicals (D_{11}), while the activity is enhanced by the higher active sites density (D_{16}) and the reduced endothermicity of the H-atom abstraction from methane (D_1). The latter corresponds with a more pronounced stability of the OH[−] species on the catalyst. Differences in oxygen chemisorption heat (D_2) are less critical for explaining the promoting effect by Sn. The beneficial role of Sn has also been reported in previous studies [14,37,38]. It seems that the presence of Sn leads to the formation of a stable mixed oxidic system Sn–Li–O which maintains a high number of active sites in the form of [Li⁺O[−]], that is, higher D_{16} , hindering the

catalytic formation of CO₂, that is, lower D_{11} [37]. Moreover, the addition of Sn to Li/MgO increases the acidity of the catalyst surface and induces a stronger binding of the hydroxyl anions to the acidic surface cation sites, that is, lower D_1 . It is widely accepted that hard bases, such as OH[−], prefer to interact with hard acids, like Sn⁺⁴, due to strong electrostatic interactions [39]. It is worth mentioning at this point that the activity enhancement by a hard acid as Sn, although being valid for the Li/MgO catalyst family, may not be generally valid. For example, it is possible that within a range of catalyst descriptors, values differing from those corresponding to (Sn)Li/MgO (see Table 5) enhancing the catalyst acidity may have less pronounced or even an inverse effect.

Further analysis of the values of the catalyst descriptors presented in Table 5 can explain the higher methane conversion attained with Sr/La₂O₃ than with Sn–Li/MgO catalyst. Indeed, the former catalyst has a higher active site density, D_{16} , and exhibits an even less endothermic Eley–Rideal methane H-atom abstraction step, D_1 . The chemisorption heat of hydroxyls on the surface of Sr/La₂O₃ was calculated to amount to approximately 278 kJ/mol, while the corresponding value for Sn–Li/MgO was nearly 266 kJ/mol. Furthermore, the higher O₂ chemisorption heat, D_2 , indicates stronger bonding of atomic oxygen to the surface of the Sr/La₂O₃ catalyst and, hence, larger contribution of the catalytic reaction network to the overall OCM reaction, since atomic oxygen is involved in a large number of catalytic steps (see Table 2). This effectively promotes methane activation over Sr/La₂O₃, yet it also boosts surface carbon dioxide formation, which is further enhanced by the high sticking coefficient of methyl radicals on the surface of the Sr/La₂O₃ catalyst (see Table 2).

Given the differences in operating conditions used in the determination of the OCM kinetics, an unequivocal comparison among the various catalysts is only feasible via microkinetic modelling. For this purpose, the experimental points produced over Sr/La₂O₃ shown in Fig. 5 were simulated by the model employing the descriptor values pertaining to the Li/MgO and Sn–Li/MgO catalysts (see Table 5). As shown in Fig. 8, methane conversion over Sr/La₂O₃ catalyst is simulated approximately 5 and 33 times higher than over the Sn–Li/MgO and Li/MgO catalysts, respectively, under identical operating conditions described in Section 3.1.2. At a space time equal to 0.35 kg s mol^{−1} reactants, Sr/La₂O₃ and Li/MgO exhibit a similar selectivity to C₂ products of about 25%, with the former catalyst being much more active. A much higher C₂ selectivity, amounting to 70% is simulated for Sn–Li/MgO compared to only 25% over Sr/La₂O₃ irrespective of the applied

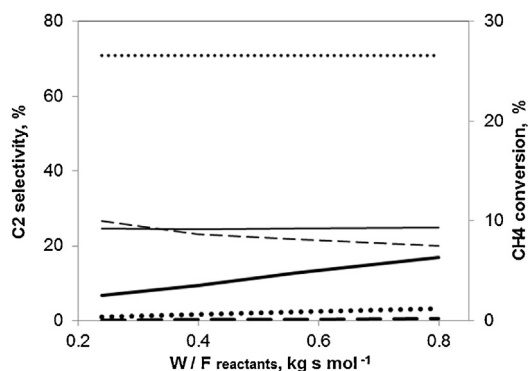


Fig. 8. Simulated CH_4 conversion and C_2 selectivity vs. space time. Conversions, thick lines; selectivities, thin lines; (dashed line) Li/MgO ; (dotted line) Sn-Li/MgO ; (full line) $\text{Sr/La}_2\text{O}_3$; operating conditions: $T = 1023 \text{ K}$, $p = 190 \text{ kPa}$, inlet molar CH_4/O_2 ratio = 4, N_2 dilution: 80%. Simulation results were obtained with the model described in Section 2.2 and the values of E_0 and catalyst descriptors are listed in Tables 4 and 5, respectively.

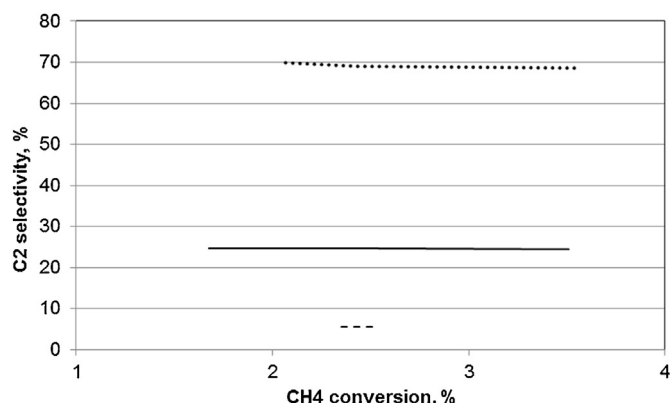


Fig. 9. Simulated C_2 selectivity vs. CH_4 conversion. (dashed line) Li/MgO ; (dotted line) Sn-Li/MgO ; (full line) $\text{Sr/La}_2\text{O}_3$; Operating conditions: $T = 1023 \text{ K}$, $p = 190 \text{ kPa}$, inlet molar CH_4/O_2 ratio = 4, N_2 dilution: 80%. Simulation results were obtained with the model described in Section 2.2 and the values of E_0 and catalyst descriptors are listed in Tables 4 and 5, respectively.

space time, under the investigated conditions. Fig. 9 presents the C_2 selectivity as a function of methane conversion so that a more concrete comparison can be made among the catalysts with respect to C_2 selectivity. As clearly seen under operating conditions that lead to similar CH_4 conversion, that is, 2.5%, by employing the micro kinetic model, the three catalysts are ranked with respect to selectivity as follows from high to low: $\text{Sn-Li/MgO} > \text{Sr/La}_2\text{O}_3 > \text{Li/MgO}$.

4. Conclusions

The adequate description of OCM kinetic data on an extended range of catalysts, that is, a novel investigated 1 wt% $\text{Sr/La}_2\text{O}_3$ and two literature-reported (Sn/Li/MgO) catalysts, required the incorporation of additional, heterogeneously catalyzed oxidation reaction steps toward CO_2 in the previously developed, comprehensive microkinetic model. The good agreement between simulated and experimental results on all three investigated catalysts is especially noteworthy, as the current model enables the generic description of reaction performances based on a single reaction network. The $\text{Sr/La}_2\text{O}_3$ catalyst was found to be more active than the Li-based catalysts, while the Sn-Li/MgO proved to be the most

selective catalyst toward C_2 products. Using the model, it was shown that the catalyst descriptors which control the activity are: (1) the reaction enthalpy of methane H-atom abstraction associated with the hydroxyl radical chemisorption enthalpy, (2) the oxygen chemisorption enthalpy, and (3) active site density. Likewise, the catalyst descriptors governing the C_2 selectivity are the oxygen chemisorption enthalpy and methyl radical sticking coefficient. The above analysis demonstrates that a microkinetic model including catalyst descriptors is a useful tool in the assessment of experimental data on a wide range of catalysts.

Acknowledgement

This article reports the work undertaken in the context of the project “OCMOL, Oxidative Coupling of Methane followed by Oligomerization to Liquids.” OCMOL is a large-scale collaborative project supported by the European Commission in the 7th Framework Programme (GA n 228953). For further information about OCMOL, see <http://www.ocmol.eu>.

References

- [1] G.E. Keller, M.M. Bhasin, *J Catal* 73 (1982) 9.
- [2] P.M. Couwenberg, Q. Chen, G.B. Marin, *Ind Eng Chem Res* 35 (1996) 3999.
- [3] P.M. Couwenberg, Q. Chen, G.B. Marin, *Ind Eng Chem Res* 35 (1996) 415.
- [4] V.R. Choudhary, S.A.R. Mulla, V.H. Rane, *J Chem Technol Biot* 71 (1998) 167.
- [5] S. Arndt, T. Otremba, U. Simon, M. Yildiz, H. Schubert, R. Schomacker, *Appl Catal A-Gen* 425 (2012) 53.
- [6] J.X. Wang, L.J. Chou, B. Zhang, H.L. Song, J. Zhao, J. Yang, S.B. Li, *J Mol Catal A-Chem* 245 (2006) 272.
- [7] L.J. Chou, Y.C. Cai, B. Zhang, J.Z. Niu, S.F. Ji, S.B. Li, *React Kinet Catal L* 76 (2002) 311.
- [8] L.J. Chou, Y.C. Cai, B. Zhang, J.Z. Niu, S.F. Ji, S.B. Li, *Appl, Catal A-Gen* 238 (2003) 185.
- [9] W. Zheng, D.G. Cheng, N. Zhu, F.Q. Chen, X.L. Zhan, *J Nat Gas Chem* 19 (2010) 15.
- [10] K. Huang, X.L. Zhan, F.Q. Chen, D.W. Lu, *Chem Eng Sci* 58 (2003) 81.
- [11] W. Zheng, D.G. Cheng, F.Q. Chen, X.L. Zhan, *J Nat Gas Chem* 19 (2010) 515.
- [12] M. Boudart, *Catal Lett* 65 (2000) 1.
- [13] J.W. Thybaut, J.J. Sun, L. Olivier, A.C. van Veen, C. Mirodatos, G.B. Marin, *Catal Today* 159 (2011) 29.
- [14] J. Sun, J.W. Thybaut, G.B. Marin, *Catal Today* 137 (2008) 90.
- [15] L. Mleczko, M. Baerns, *Fuel Process Technol* 42 (1995) 217.
- [16] Q. Chen, J.H.B.J. Hoebink, G.B. Marin, *Ind Eng Chem Res* 30 (1991) 2088.
- [17] Q. Chen, P.M. Couwenberg, G.B. Marin, *Aiche J* 40 (1994) 521.
- [18] P.N. Kechagiopoulos, J.W. Thybaut, G.B. Marin, *Ind Eng Chem Res* (2013), <http://dx.doi.org/10.1021/ie403160s>.
- [19] V.R. Choudhary, S.A.R. Mulla, V.H. Rane, *J Chem Technol Biot* 72 (1998) 125.
- [20] L. Olivier, S. Haag, H. Pennemann, C. Hofmann, C. Mirodatos, A.C. van Veen, *Catal Today* 137 (2008) 80.
- [21] Q. Chen, P.M. Couwenberg, G.B. Marin, *Catal Today* 21 (1994) 309.
- [22] M.Y. Sinev, Z.T. Fattakhova, V.I. Lomonosov, Y.A. Gordienko, *J Nat Gas Chem* 18 (2009) 273.
- [23] M.I. Temkin, *Int Chem Eng* 11 (1971) 709.
- [24] Z.M. Gao, Y.Y. Ma, *J Nat Gas Chem* 19 (2010) 534.
- [25] N. Schumacher, A. Boisen, S. Dahl, A.A. Gokhale, S. Kandori, L.C. Grabow, J.A. Dumesic, M. Mavrikakis, I. Chorkendorff, *J Catal* 229 (2005) 265.
- [26] Y.S. Su, J.Y. Ying, W.H. Green, *J Catal* 218 (2003) 321.
- [27] A.B. Mhadeshwar, H. Wang, D.G. Vlachos, *J Phys Chem B* 107 (2003) 12721.
- [28] A. Michaelides, Z.P. Liu, C.J. Zhang, A. Alavi, D.A. King, P. Hu, *J Am Chem Soc* 125 (2003) 3704.
- [29] J.A. Dumesic, D.F. Rudd, *The microkinetics of heterogeneous catalysis*, American Chemical Society, Washington, DC, 1993.
- [30] O.V. Krylov, *Catal Today* 18 (1993) 209.
- [31] H.H. Rosenbrock, *J Comput* 3 (1960) 175.
- [32] P.T. Boggs, J.R. Donaldson, R.H. Byrd, R.B. Schnabel, *Acem T Math Software* 15 (1989) 348.
- [33] M. Casarin, D. Falcomer, A. Glisenti, A. Vittadini, *Inorg Chem* 42 (2003) 436.
- [34] V.E. Ostrovskii, *Thermochim Acta* 489 (2009) 5.
- [35] J. Majzlan, L. Mazeina, A. Navrotsky, *Geochim Cosmochim Acta* 71 (2007) 615.
- [36] Y.P. Arnaud, *Appl Surf Sci* 62 (1992) 37.
- [37] K. Nagaoka, T. Karasuda, K. Aika, *J Catal* 181 (1999) 160.
- [38] E.P.J. Mallens, J.H.B.J. Hoebink, G.B. Marin, *J Catal* 160 (1996) 222.
- [39] M.W. Abee, D.F. Cox, *Surf Sci* 520 (2002) 65.